Biosensors and Bioelectronics 117 (2018) 794–801

Contents lists available at ScienceDirect

Biosensors and Bioelectronics

journal homepage: www.elsevier.com/locate/bios

Construction and characterization of a theranostic system based on graphene/manganese chelate

Reza Karimi Shervedani[a,*], Marzieh Samiei Foroushani[a], Amirhosein Kefayat[b], Mostafa Torabi[a], Fatemeh Rahnemaye Rahsepar[a]

[a] Department of Chemistry, University of Isfahan, Isfahan 81746-73441, Iran
[b] Cancer Prevention Research Center, Isfahan University of Medical Sciences, Isfahan 81746-73461, Iran

ARTICLE INFO

Keywords:
Theranostic
Graphene oxide
Anticancer drug
Mn(II) complex
Contrast agent
Albumin

ABSTRACT

Construction of hybrid systems that combine the cancer treatment and diagnosis agents on a single platform, known as theranostic systems, have received great attentions in the field of nanobiomedicine. Here, construction and characterization of a new multifunctional hybrid theranostic system based on RGO, PDA, BSA, DTPA-Mn(II), and MTX constituents, is presented. Accordingly, GO is partially reduced and simultaneously functionalized by dopamine, leading to reduced graphene oxide/polydopamine, RGO-PDA system; and then, the bovine serum albumin protein (BSA) is grafted onto this system. The obtained system, RGO-PDA-BSA, is further decorated with diethylenetriaminepentaacetic acid-Mn(II) as diagnostic system and methotrexate as anticancer drug. Physicochemical characteristics of the RGO-PDA-BSA-DTPA-Mn(II)/MTX system are studied by Fourier transform infrared spectroscopy, atomic force microscopy, and electrochemical methods. The capturing ability of the prepared system for the cancer cells is evaluated through electrochemical impedance spectroscopy (EIS) and by using the 4T1 cancer cells in comparison with L929 normal cells. The EIS results indicate that a degree of selectivity as 6.23 for GC-RGO-PDA-BSA-DTPA-Mn(II)/MTX electrode system toward 4T1 cells, which is larger than that obtained for this system toward the L929 cells. Similar analysis performed using the GC-RGO-PDA-DTPA-Mn(II)/MTX system (having no BSA) indicate that the selectivity degree of the system is increased only by a factor of 1.6, implying that presence of BSA has increased the selectivity of the system for 4T1 cells by a factor of four. This behavior supports the crucial role of BSA in this process for 4T1 cells. Finally, the drug release study of RGO-PDA-BSA-DTPA-Mn(II)/MTX system is performed successfully at pH 7.4.

1. Introduction

Theranostic nanomedicines, consisting of both diagnostic and therapeutic components, have received considerable attention in recent years (Jokerst and Gambhir, 2011). These nanosystems can monitor the progression of malignant tumors, and provide treatment simultaneously. Development of nanocarriers possessing imaging probe and therapeutic agents with unique biological property is the crucial basis of theranostic nanomedicine (Burger et al., 2002; Ke et al., 2011; Lu et al., 2007). Recently, great efforts have been allocated to apply graphene-based materials in the biomedical fields such as cancer therapy, medical imaging and drug delivery because of unique physical and biological properties of these materials (Feng and Liu, 2011; Yang et al., 2013, 2015; Zhang et al., 2013).

Magnetic resonance imaging (MRI) as a powerful noninvasive technique has been routinely used in medical imaging. However, due to the innate low sensitivity of MRI, the T_1 and T_2 MRI contrast agents (CAs) are frequently used to achieve precise and reliable diagnosis of pathologic changes (Zhang et al., 2013). Still, due to the low sensitivity and rapid excretion in vivo of many of the available CAs, metal ion based hybrid systems have been designed to improve the relaxivity (r_1) of the proton of nearby water molecules and provide more selective tissue uptake (Kueny-Stotz et al., 2012; Gianolio et al., 2012; Zhang et al., 2013). Although gadolinium (Gd) based T_1 CAs have long been used in MRI imaging because of Gd paramagnetic properties, the discovery of its potential toxicity has driven the researchers to design and develop the novel MRI CAs with low toxicity, high sensitivity and efficiency, and the ability in cellular imaging based on other paramagnetic metals (Kueny-Stotz et al., 2012; Pan et al., 2008). Therefore, some other metal-ion paramagnetic complexes, which are promising to have more desirable properties, for example the Mn-based compounds like diethylenetriaminepentaacetic acid (DTPA)-Mn(II), have been

* Corresponding author.
E-mail address: rkarimi@sci.ui.ac.ir (R. Karimi Shervedani).

https://doi.org/10.1016/j.bios.2018.07.011
Received 22 March 2018; Received in revised form 8 July 2018; Accepted 9 July 2018
Available online 10 July 2018
0956-5663/

studied as MRI T_1 contrast agents (Pan et al., 2008, 2011).

The unique properties of graphene such as large surface area to load MRI probes, prolonging the half-life of MRI contrast agents in vivo and its surface functionalization with targeting groups make it an excellent candidate for the synthesis of MRI hybrid contrast agents (Zhang et al., 2013; Shen et al., 2012). Moreover, the large molecular weight of the graphene oxide (GO) system can slow down the rotational motion of the water proton, leading to enhanced T_1 relaxivity and imaging contrast (Zhang et al., 2013).

The present work is intended to design, construct, and study a multifunctional hybrid system based on RGO, PDA, BSA, DTPA-Mn(II), and MTX constituents, and then, test it for 4T1 cells. First, the GO is synthesized (Hummers and Offeman, 1958) and functionalized with polydopamine (PDA) by self-polymerization of dopamine (DA) (Liu et al., 2014). The DA is used as a reducing as well as functionalizing agent for GO to form RGO-PDA. The PDA film stabilizes and protects the RGO, acts as the anchor to graft bovine serum albumin (BSA) biopolymer onto the RGO-PDA surface via Michael addition and/or Schiff base reactions (using thiols and amines groups present on BSA) to form RGO-PDA-BSA system (Cheng et al., 2013).

Regarding the role of BSA, three points should be mentioned here: (i) In general, albumins are highly promising drug carrier in drug delivery systems due to their high consumption in solid tumors and in inflammation sites (Frei, 2011; Kratz, 2008). (ii) BSA has played an antifouling role to block excess active sites of the biosensors platforms like graphene and to avoid the nonspecific adsorptions of unwanted species on the surface of biosensors (Wang et al., 2015). (iii) The BSA had been previously applied as a macromolecular carrier for the paramagnetic agents (Ogan et al., 1987; Schmiedl et al., 1987). Therefore, the utilization of RGO-PDA-BSA system for therapy intentions and immobilization of paramagnetic agents for applying in diagnostic intentions seems reasonable. At least, there are two ways to start with BSA for this system: (a) using BSA as carrier for paramagnetic agents in the molecular scale, e.g. BSA-DTPA-Mn(II) and (b) using BSA as micro/nanoparticles (NPs) platform for this purpose, BSA-DTPA-Mn(II) NPs. Clearly, the case (a) is not the purpose of the current work. For the case (b), the BSA NPs, reported till now (Kratz, 2008), have exposed lower surface area, and thus, lower loading capacity, compared with the GO (or RGO) (Cheon et al., 2016). Thus, nanostructure systems include BSA in conjunction with RGO can offer interesting effects for theranostic systems.

Preparation and water relaxation properties of proteins labeled with paramagnetic metal chelates; the BSA-EDTA-Mn(II) and BSA-DTPA-Mn (II) systems, have already been reported (Lauffer and Brady, 1985). However, to the best of our knowledge, there is no previous report on the interaction of RGO-PDA-BSA system with the complex of DTPA-Mn (II), a paramagnetic complex used as a cancer cells diagnostic agent in drug systems (Pan et al., 2011).

In the current work, DTPA is conjugated with RGO-PDA-BSA, followed by complexation with Mn(II) ions, to construct RGO-PDA-BSA-DTPA-Mn(II) system. The obtained system is used to load methotrexate (MTX, a model of anticancer drug). To evaluate the capturing ability of the system for the cancer cells, the mouse breast cancer cells 4T1 are examined as a model, in comparison with mouse fibroblast L929 normal cells (Aravind et al., 2012). The capturing process is traced by electrochemical methods.

2. Methods and materials

To save the space and benefits of the result, the sections related to materials and reagents, cell culture, and the instruments applied for topography and structural studies of the systems surfaces are presented in Supplementary Data file, Sections S1 to S3.

2.1. Graphene surface modification

2.1.1. Synthesis of GO

The GO was synthesized according to the Hummers' method (Hummers and Offeman, 1958) partially modified by us (Karimi Shervedani et al., 2017a).

2.1.2. Synthesis of RGO-PDA

In a typical system, a 100.0 mg of the GO was dispersed into a 200.0 mL of PBS, pH 8.5, by using an ultrasonic bath (FLAC, LBS2: 60 kHz, Italy) to create a homogeneous suspension solution. Then, a 50.0 mg of DA was added into the suspension solution and the mixture was stirred magnetically at 60 °C for an optimal time of 24 h (Fig. S1). The formed RGO-PDA was purified by distilled water via centrifuging at 8000 rpm four times (4 × 50 mL) to remove extra DA. The obtained powder was dried at 70 °C and used for next modification steps (Xu et al., 2010).

2.1.3. Synthesis of RGO-PDA-BSA

RGO-PDA-BSA was prepared as following: A 100.0 mg of RGO-PDA was redispersed into 200.0 mL PBS, pH 8.5, by sonication for 10 min, then, 50.0 mg BSA was added. The grafting reaction of BSA on RGO-PDA was carried out at room temperature for 24 h with magnetically stirring to reach the maximum BSA grafting amount (Cheng et al., 2013). Afterwards, the solution was centrifuged (8000 rpm) and washed thoroughly with distilled water four times to remove the unbounded BSA. The obtained powder was dried at 70 °C and used for next modification steps.

2.1.4. Synthesis of RGO-PDA-BSA-DTPA-Mn(II)

RGO-PDA-BSA-DTPA was synthesized according to a modified procedure presented in the literature (Zhang et al., 2013). First; a solution containing 0.500 g DTPA, 0.250 g EDC and 250.0 μL triethylamine (TEA) was prepared in 25.0 mL dimethylsulfoxide (DMSO) and vigorously stirred in darkness for 3 h to activate carboxylic acid groups of DTPA. Then, a 100.0 mg sample of RGO-PDA-BSA powder was suspended in this solution; the mixture was sonicated for 10 min and then, allowed to stir overnight. Finally, the RGO-PDA-BSA-DTPA was purified and separated as powder by washing with distilled water and drying at 70 °C.

Complexation of Mn(II) was performed as follows: a 100.0 mg sample of RGO-PDA-BSA-DTPA powder was suspended in a 50.0 mL of distilled water and its pH adjusted to ~ 6.0 (Schwendener et al., 1989) by HC1 and the mixture was sonicated for 10 min. Then, the $MnCl_2$ sample was added to mixture under stirring so that its final concentration was 20.0 mM. The purification was carried out based on above-mentioned method.

Presence of Mn(II) ions adsorbed on the system was supported by electrochemical method, however, total amount of Mn(II) ions of the system was measured by using atomic absorption spectroscopy (AAS) (Shilina et al., 2016) according to the method presented in Supplementary Data file, Section S5.

2.1.5. Loading of anticancer drug on RGO-PDA-BSA-DTPA-Mn(II)

A sample of RGO-PDA-BSA-DTPA-Mn(II) powder was mixed with an aqueous solution of MTX, pH 7.0, so that the mass ratio of MTX to the powder was 2:1. Then, the solution mixture was sonicated for 10 min to obtain a homogeneous suspension solution and stirred in dark at room temperature for 24 h to reach a maximum loading of MTX. The free MTX was removed by distilled water via centrifuging. The concentration of MTX loaded on the RGO-PDA-BSA-DTPA-Mn(II) was determined by using a calibration curve constructed based on UV–Vis absorbance peak at 290 nm (Figs. S2 to S4). The loading ratio refers to the weight ratio of MTX to GO (Zhang et al., 2013).

2.1.6. Control experiments

Several systems were prepared and examined in the same way explained above, but without BSA including RGO-PDA-DTPA, RGO-PDA-DTPA-Mn(II) and RGO-PDA-DTPA-Mn(II)/MTX to elucidate the role of BSA.

2.2. In-vitro MTX release from RGO-PDA-BSA-DTPA-Mn(II)/MTX

The release profile of MTX from RGO-PDA-BSA-DTPA-Mn(II)/MTX was carried out in PBS media at pH 7.4 and 37 °C, the samples were filtered through a dialysis bag (MWCO: 14 kDa) at the different time intervals, and the concentration of the released MTX drug was measured by UV–Vis spectroscopy.

2.3. Electrochemical measurements

Modification of GC electrode surface by graphene based samples, numbered as (i) to (vi) (Section 2.1), and electrochemical study the capturing ability of the constructed systems toward the 4T1 cancer cells have been presented in Supplementary Data file, Section S7.

3. Results and discussion

3.1. Preparation of RGO-PDA-BSA-DTPA-Mn(II) system

Synthesis of RGO-PDA-BSA-DTPA-Mn(II) system is outlined in Scheme 1. Briefly, (i) the GO nanosheets (Karimi Shervedani et al., 2017a), is mixed with DA (pH 8.5, 60 °C), and the mixture is vigorously stirred. The DA has several interesting properties such as self-polymerization, adhesion, biocompatibility, and reducing power (Hong et al., 2011). The formed PDA stabilizes the GO against agglomeration and fouling effects, attenuates the in vivo toxicity of GO, and functionalizes its surface for further modification. In effect, GO is reduced to RGO by DA, and DA is converted to PDA, consequently, RGO-PDA is formed (Cheng et al., 2013). Many functional groups, such as catechol, amine, and imine, which are available on RGO-PDA surface, serve as the starting sits for covalent modification of the surface with desired molecules such as proteins and organic ligands (Cheng et al., 2013; Liu et al., 2014). (ii) Albumin is a major energy and nutrition source for tumor growth. Accumulation of albumin in solid tumors and high albumin consumption at sites of inflammation are caused to use it as a drug carrier in the clinical setting (Kratz, 2008). Moreover, albumin has been applied as a macromolecular carrier for the paramagnetic agents to increase efficiency in proton relaxation enhancement (Ogan et al., 1987; Schmiedl et al., 1987). Albumin has a large number of lysine residues through which a large number of paramagnetic agents can be covalently coupled with it (Ogan et al., 1987; Schmiedl et al., 1987). For these reasons, the BSA is used as a model of serum albumin, and grafted onto RGO-PDA surface by means of catechol chemistry (no chemical activator is used) (Cheng et al., 2013; Liu et al., 2014). (iii) The DTPA, usually used as a therapeutic agent (Ding et al., 2006), is covalently immobilized onto RGO-PDA-BSA surface (via chemical reaction between –COOH groups of DTPA and $–NH_2$ groups of the surface using EDC activator to bring DTPA onto the surface system), forming the RGO-PDA-BSA-DTPA platform for accumulation of Mn(II). Thus, RGO-PDA-BSA-DTPA powder was added to the Mn(II) solution, resulting in the RGO-PDA-BSA-DTPA-Mn(II) as a carrier system for MTX drug (Section 2.1).

For comparison, RGO-PDA-DTPA and RGO-PDA-DTPA-Mn(II) systems (having no BSA) are also prepared and tested in the same way.

Finally, the MTX was transferred onto the systems at appropriate conditions, and examined for cancer cells.

3.2. Surface morphology and structure characterization

3.2.1. Characterization by FTIR

The FTIR spectroscopy measurements (Fig. 1) are performed to support step-by-step attachment of modifying layers onto the GO surface.

The FTIR spectrum of GO surface (curve a) shows stretching vibrations of C-O, C-OH, C=C, C=O and O-H, respectively, at 1098, 1367, 1618, 1727 and 3400 cm^{-1} (Karimi Shervedani et al., 2017b). After functionalization of GO with PDA, the intensity of these peaks decreases significantly, suggesting that the amount of oxygen-containing groups at the surface of GO are greatly reduced (curve b). Moreover, some new peaks are observed at 768, 1210, and 1576 cm^{-1} on RGO-PDA spectrum, which are corresponded to the vibrations of N-H wagging, C-N stretching (aliphatic amines), and the aromatic ring mode of PDA, respectively (Zangmeister et al., 2013; Gu et al., 2013). These results support the successful modification of PDA on RGO sheets.

The new absorption peak appeared around 1382 cm^{-1} upon immobilization of BSA on the RGO-PDA surface (curve c) is attributed to the C-N-H vibration (Amide III band) mode (Barth, 2007), supporting the existence of BSA on the surface. It should be noted that the major vibration peaks associated with the Amides I (~ 1650 cm^{-1}) and II

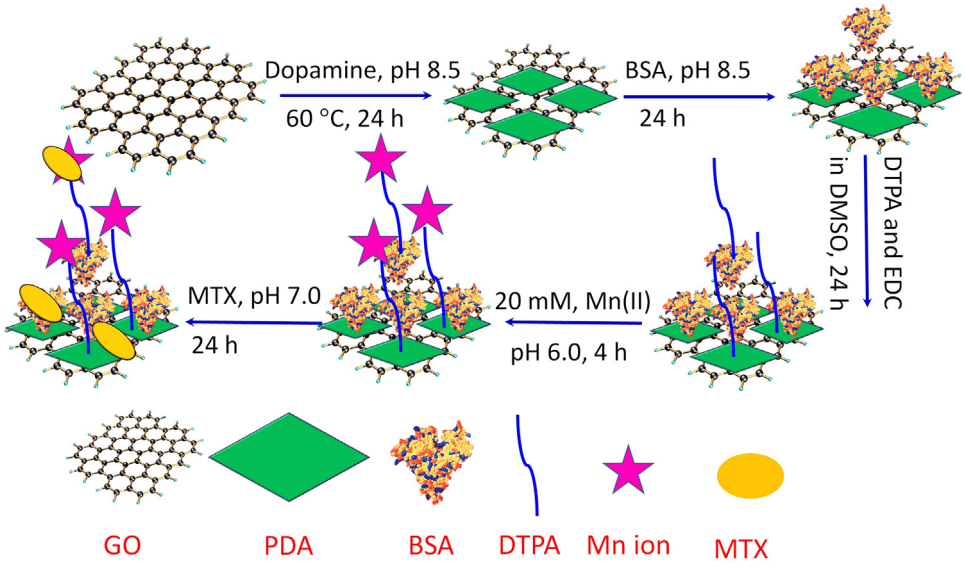

Scheme 1. Schematic illustration for step-by-step modification of GO surface by PDA, BSA, DTPA-Mn(II), and MTX constituents.

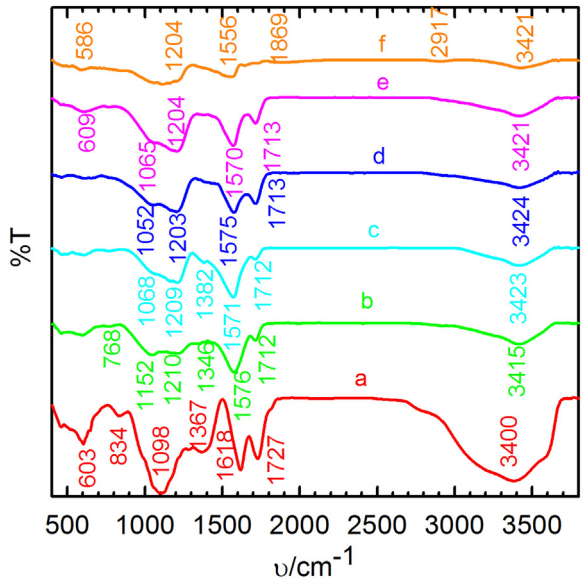

Fig. 1. FTIR spectra obtained on the (a) GO, (b) RGO-PDA, (c) RGO-PDA-BSA, (d) RGO-PDA-BSA-DTPA, (e) RGO-PDA-BSA-DTPA-Mn(II), and (f) RGO-PDA-BSA-DTPA-Mn(II)/MTX surfaces.

(~ 1550 cm^{-1}) bands of BSA could not be distinguished because they are probably overlapped with the broad peak of RGO-PDA appeared around 1576 cm^{-1}. Upon grafting of DTPA onto the RGO-PDA-BSA surface, the intensity of C-O, C-N, and C = O bands, appeared around 1052, 1203, and 1713 cm^{-1}, respectively, is increased significantly, especially the peak of C = O (curve d). Complexation of Mn(II) ion by the system, RGO-PDA-BSA-DTPA-Mn(II), leads to a decrease in the C = O intensity around 1713 cm^{-1} (curve e). It should be noted that the intensity of the bands appeared around ~1065, 1204 and 1570 cm^{-1} increases significantly. This increase can be explained based on the resonance in the created complex rings and consequently changes in the length of C–O and C–N bonds (Karimi Shervedani et al., 2016).

Immobilization of MTX onto the surface, RGO-PDA-BSA-DTPA-Mn (II)/MTX, causes considerable changes in the intensity and frequency of vibrational bands of the surface, and appearance of new bands (curve f). Briefly; (i) The intensity of the peaks at 1713, 1570, and 1204 cm^{-1} are deceased which is a resultant of deeper position of the related groups in the RGO-PDA-BSA-DTPA-Mn(II)/MTX structure (negative effect) that causes more loss of the incident and reflected IR rays, and the presence of MTX on the system (positive effect). (ii) A new vibrational band is appeared around 1869 cm^{-1}, which is attributed to pteridine ring of MTX (Mason, 1955). Overall, this behavior supports presence of MTX immobilized on the top of the system via different possible interactions (Karimi Shervedani and Samiei Foroushani, 2014).

Control experiment. Upon direct attachment of activated DTPA onto RGO-PDA system (in the absence of BSA), the intensity of C = O, C-O and C-N bands increases significantly (Fig. S5, curve c), supporting immobilization of DTPA on the surface. Complexation of the Mn(II) with surface functional groups of RGO-PDA-PDTA system, causes some changes in the vibrational frequencies of the observed peaks (curve d), and also a decrease in the intensity of C = O and C-OH bands, appeared around 1712 and 1382 cm^{-1}. This behavior supports the complexation of Mn(II) with DTPA functions. The immobilization of MTX on RGO-PDA-DTPA-Mn(II) surface leads to the changes similar to those observed for MTX immobilization on RGO-PDA-**BSA**-DTPA-Mn(II) surface (in the presence of BSA, curve e).

These results also indicate that the presence of BSA does not prevent the immobilization of DTPA-Mn complex on the graphene surface; however, performance of BSA will be subsequently discussed. This effect is interesting and will be discussed later in Section 3.3.

Overall, the FTIR results support successful attachment of DTPA-Mn onto graphene surface and the interaction of the constructed systems with MTX.

3.2.2. Characterization by AFM

Topographical AFM images and their corresponding height analysis were used to characterize the surface morphology and the thickness of the GO and RGO nanosheets modified with PDA, BSA, DTPA, Mn(II), and MTX. Analysis of the GO images shows flat nanosheets with some wrinkles (Fig. 2A) and thickness of 3.88 nm. The PDA distributed on both sides of the RGO sheets causes the interlayer spacing to increase to 9.46 nm (Fig. 2B). The AFM image and height analysis of RGO-PDA-BSA reveal that not only the thickness is increased by about 17 nm upon attachment of BSA on RGO-PDA sheets, but also agglomerated BSA protein particles (Bausch and Leuenberger, 1994) with a thickness of about 91 nm are formed on the nanosheets (Fig. 2C).

However, the adhered DTPA could play an important role as a *disaggregating* agent to separate the agglomerated BSA proteins to the individual BSA molecules with a thickness of about 13.58 nm (Fig. 2D) (Peters, 1985). The height profile of RGO-PDA-BSA-DTPA system show that the DTPA is attached directly to RGO-PDA sheets (immobilization of Mn(II) on the system did not change the AFM signals significantly, and thus, no AFM data is presented for this case). Loading of MTX on RGO-PDA-BSA-DTPA-Mn(II) surface forms almost a smooth surface with a good distribution of Mn(II)/MTX layers having a thickness of about 0.9 nm (Fig. 2E).

Control experiments; The AFM image recorded on RGO-PDA-DTPA system (i.e. in the absence of BSA), is presented in Fig. S6A. Immobilization of DTPA onto RGO-PDA sheet increases the thickness by 11.1 nm (Fig. S6A), indicating that DTPA is directly attached to the RGO-PDA sheets. The AFM image of RGO-PDA-DTPA-Mn(II)/MTX (Fig. S6B) shows that Mn(II)/MTX layers are uniformly distributed on RGO-PDA-DTPA surface just similar to RGO-PDA-BSA-DTPA-Mn(II)/MTX system (Fig. 2E). This effect is also interesting regarding targeting efficiency of RGO-PDA-BSA-DTPA-Mn(II)/MTX system. This issue will be discussed subsequently in Section 3.3.

3.2.3. Characterization by electrochemical methods

The constructed systems were also transferred onto the GC electrode surface and characterized by electrochemical methods; first indirectly based on external redox reaction of the $[Fe(CN)_6]^{3-/4-}$ probe (Fig. S7), and then, directly based on Mn(III)/Mn(II) redox reaction current (Fig. 3).

3.2.3.1. Indirect characterization. The voltammograms and impedance data obtained on the (a) clean bare GC, (b) GC-GO, (c) GC-RGO-PDA, (d) GC-RGO-PDA-BSA, (e) GC-RGO-PDA-BSA-DTPA, (f) GC-RGO-PDA-BSA-DTPA-Mn(II) and (g) GC-RGO-PDA-BSA-DTPA-Mn(II)/MTX electrodes in the presence of $[Fe(CN)_6]^{3-/4-}$ are presented in Supplementary Data, Section S10, Fig. S7, Tables S1, S2.

Control experiments; are also conducted in the same conditions but without BSA (Fig. S8 and Tables S3, S4). The obtained results support formation of the above systems.

3.2.3.2. Direct characterization. The drug and its ancestors were transferred separately to the surface of GC electrodes and studied by electrochemical methods (without using external redox probe).

While the GC, GC-GO, GC-RGO-PDA, GC-RGO-PDA-BSA, and GC-RGO-PDA-BSA-DTPA surfaces were not electrochemically active in the applied potential window (Fig. 3A, curves a to e), GC-RGO-PDA-BSA-DTPA-Mn(II) system showed a repeatable wave at the formal potential of + 0.520 V (curve f), related to Mn(III)/Mn(II) redox system (Loving et al., 2013), indicating the presence of the immobilized Mn(II) on the electrode surface (the Mn(II) ions are not significantly adsorbed on clean bare GC, Fig. S9).

Upon adsorption of the MTX (which is electrochemically inactive in

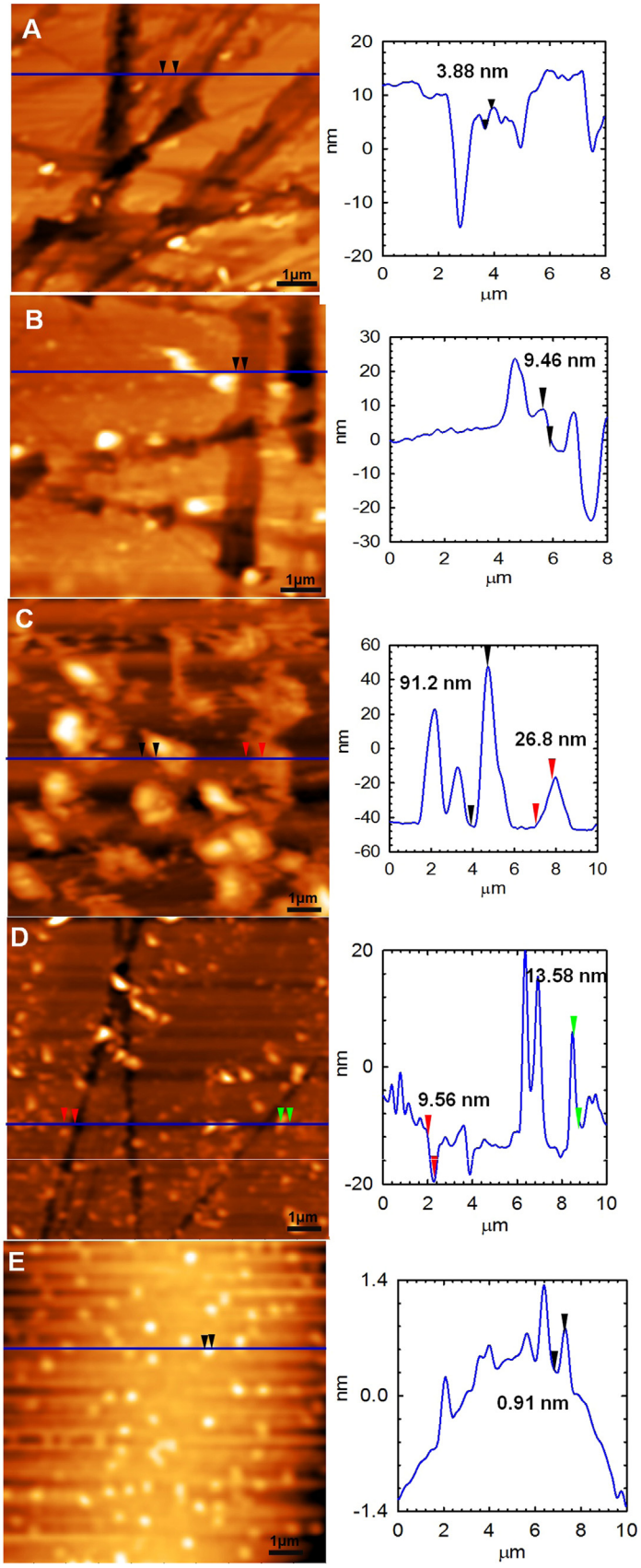

Fig. 2. AFM images and cross-section analysis of the (A) GO, (B) RGO-PDA, (C) RGO-PDA-BSA, (D) RGO-PDA-BSA-DTPA, and (E) RGO-PDA-BSA-DTPA-Mn(II)/MTX nanosystems on cleaved mica.

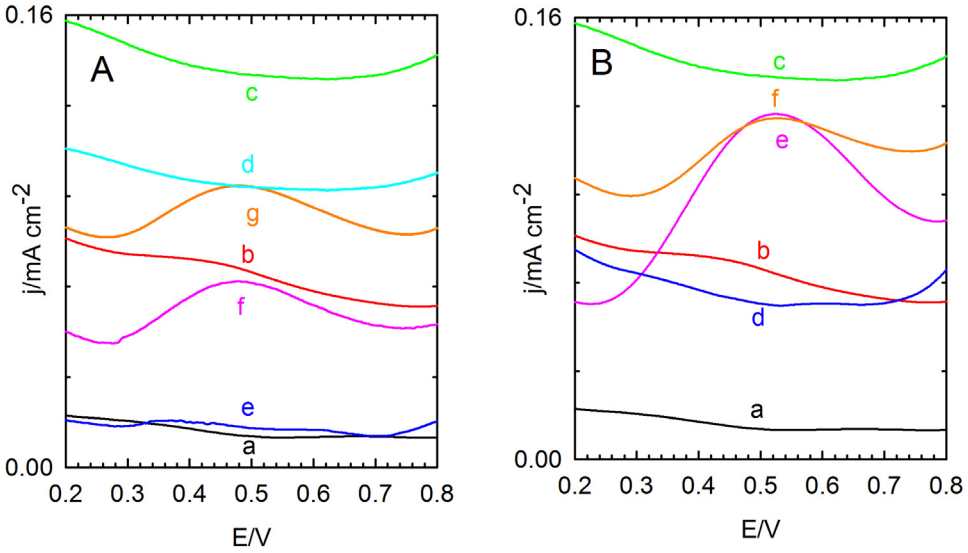

Fig. 3. Differential pulse voltammograms obtained in 0.05 M PBS, pH 7.4, in the absence of any redox probe. (A) (a) bare GC, (b) GC-GO, (c) GC-RGO-PDA, (d) GC-RGO-PDA-**BSA**, (e) GC-RGO-PDA-**BSA**-DTPA, (f) GC-RGO-PDA-**BSA**-DTPA-Mn(II) and (g) GC-RGO-PDA-**BSA**-DTPA-Mn(II)/MTX electrodes. (B) (a), (b), and (c) as in Panel (A), (d) GC-RGO-PDA-DTPA, (e) GC-RGO-PDA-DTPA-Mn(II) and (f) GC-RGO-PDA-**BSA**-DTPA-Mn(II)/MTX electrodes.

these conditions) on the RGO-PDA-BSA-DTPA-Mn system, the faradaic peak current of Mn(II) was attenuated slightly (Fig. 3A, curve g), which is a normal behavior.

One point should be explained here. The mass percent of Mn(II) in the RGO-PDA-BSA-DTPA-Mn(II)/MTX system determined (Section 2.1.iv) by AAS (Shilina et al., 2016) (1.2(± 0.5)%) indicates that an acceptable amount of Mn(II) is loaded on the composite (Pan et al., 2011). However, this value should be optimized regarding several parameters like intensity of contrast, physiological conditions and other medicinal requirements. These activities are not intended in this work.

Control experiments were performed to clarify the role of DTPA and BSA toward the Mn(II) as follows:

(i) *Role of DTPA*; the stability of Mn(II) in the system was verified through a *release experiment* (Section S3). The results indicate that a small amount of Mn(II) (~ 7%) is released from the GC-RGO-PDA-BSA-DTPA-Mn(II)/MTX system after 48 h. However, a large amount of adsorbed Mn(II) (85%) is released from the systems *contained no* DTPA in the same period of time (probably most of the Mn(II) ions have been physically adsorbed on these systems). This behavior indicates that a stable complex is formed between the Mn(II) ion and the immobilized DTPA on the system.

(ii) *Role of BSA*; the control experiments performed on the GC-RGO-PDA-DTPA, GC-RGO-PDA-DTPA-Mn(II), and GC-RGO-PDA-DTPA-Mn(II)/MTX systems (Fig. 3B), having DTPA but lacking BSA, indicate that the amount of Mn(II) had been accumulated by DTPA on the systems in the *absence* of BSA (1.4(± 0.3)%) (Panel B, curve f), is not significantly different from that accumulated in the same conditions but in the *presence* of BSA (1.2(± 0.5)%) (Panel A, curve g). The Mn(II) accumulated on these systems was also stable; a small amount (~9%) of the accumulated Mn(II) is released from the systems contained DTPA for a relatively large incubation time, 48 h (The difference observed in the currents, compared on RGO-PDA-DTPA-Mn(II) (Panel B, curve e) and RGO-PDA-BSA-DTPA-Mn (II) (Panel A, curve f), is due to part of Mn(II) ions loosely kept with free groups of PDA, which are detached by addition of MTX to the system, Panel B, curve f).

Overall, the obtained results support stability of DTPA-Mn(II) unit on both RGO-PDA and RGO-PDA-BSA systems.

3.3. Electrochemical study of interaction of the systems with 4T1 cancer cells

Interaction of RGO-PDA-**BSA**-DTPA-Mn(II)/MTX and RGO-PDA-DTPA-Mn(II)/MTX systems with 4T1 and L929 cells as models of cancer and normal mouse cells, respectively, was traced by using the EIS (Karimi Shervedani et al., 2016; Venkatanarayanan et al., 2013). The data were fitted into the appropriate equivalent circuit model (Fig. 4, Model M1), and the quantitative results were extracted (Tables S2, S4). The results show that both the systems having MTX accumulate the 4T1 cells effectively compared with L929 cells. However, precise analysis of the results shows that:

(i) The degree of selectivity of the GC-RGO-PDA-BSA-DTPA-Mn(II)/MTX electrode system, having BSA, toward 4T1 cells is 6.23 times larger than that obtained for this system toward the L929 cells {(use the ΔR_{ct} from Table S2, Rows 7–9 to obtain ($\Delta R_{ct,\ 7\&8}/\Delta R_{ct,\ 7\&9}$)}. Similar analysis performed using GC-RGO-PDA-DTPA-Mn(II)/MTX electrode system, lacking BSA {(use the ΔR_{ct} from Table S4, Rows 6–8)} resulted in a factor of 1.6. Comparison of the results shows that the degree of selectivity of the system having BSA for 4T1 cells is 4 times larger than that lacking BSA (capturing role of BSA in this process). Several reports have suggested that BSA acts as a nutrition source for tumors (Frei, 2011; Pichler et al., 2013), therefore, it can be concluded that the increased selectivity comes mainly from high albumin consumption by cancer cells.

(ii) To verify the involvement of the MTX in mediating uptake of the cells, the GC-RGO-PDA-**BSA**-DTPA-Mn(II) and GC-RGO-PDA-DTPA-Mn(II), systems having *no MTX* in their structure, were prepared and examined for 4T1 cell solutions (Fig. S10); and the ΔR_{ct} each system was extracted (Fig. 4C). Several comparisons can be made (Tables S2, S4). The relative degree of selectivity (RDS), which is more valuable to compare the efficiency of the systems toward 4T1 cells. In effect, the system having both BSA & MTX (immobilized in the neighboring on RGO-PDA system) showed the highest degree of selectivity toward the 4T1 cells;

$$RDS = [(\Delta R_{ct,\ system\ \textbf{\textit{having}}\ \textbf{both}\ BSA\ \&\ MTX\ for\ 4T1}) / (\Delta R_{ct,\ system\ \textbf{\textit{having}}\ \textbf{just}\ BSA\ for\ 4T1})] = 18.7/3.1 = 6.03$$

$$RDS = [(\Delta R_{ct,\ system\ \textbf{\textit{having}}\ \textbf{just}\ MTX\ for\ 4T1}) / (\Delta R_{ct,\ system\ \textbf{\textit{lacking}}\ \textbf{both}\ BSA\ \&\ MTX\ for\ 4T1})] = 9.8/4.3 = 2.2$$

These results, the strong interaction with the 4T1 cells, besides other

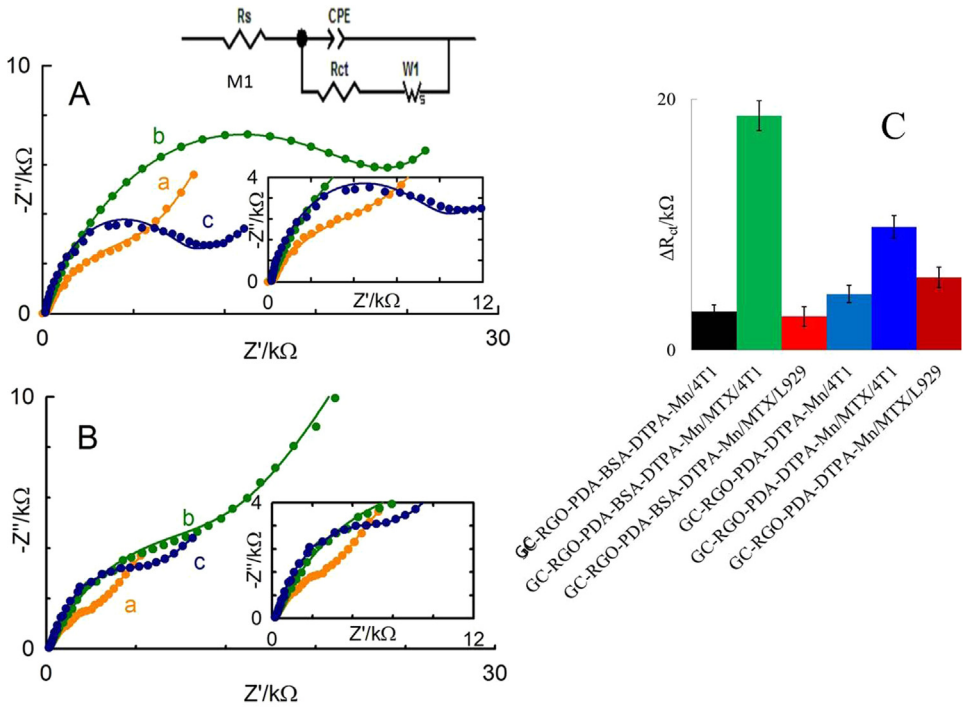

Fig. 4. The EIS complex plane plots obtained on; (A) RGO-PDA-BSA-DTPA-Mn(II)/MTX and (B) RGO-PDA-DTPA-Mn(II)/MTX electrodes (a) before and after incubating in 10^5 cell/mL (b) 4T1 and (c) L929 cells. Incubation time 30 min; pH 7.4. Measurement conditions; sterile PBS, pH 7.4, 5.0 mM $[Fe(CN)_6]^{3-/4-}$, E_{DC} = +0.200 V (vs. Ag/AgCl), E_{AC} = 5 mV, and frequency range 10 kHz to 0.1 Hz. (C) Histogram presenting charge-transfer resistance obtained in 0.05 M PBS at pH 7.4 in the presence of 5.0 mM $[Fe(CN)_6]^{3-/4-}$ on different graphene modified surfaces. Error bars are obtained using at least three measurements.

interesting properties like biocompatibility, large surface area, ease functionalization and stable physicochemical properties show that the system has several benefits for theranostic intentions.

3.4. In-vitro release study of MTX

According to the above findings, the RGO-PDA-BSA-DTPA-Mn(II) system can be suggested as a drug delivery platform. Therefore, the efficiency of the system for this propose is studied by the drug release experiments of RGO-PDA-BSA-DTPA-Mn(II)/MTX. The amount of MTX loaded by the system was found as 21(± 5) mass% (Section 2.2). The results show that about 80% of MTX has been released from the systems during the first 12 h of incubation time at pH 7.4, with essentially no further release for longer times (Fig. 5).

4. Conclusion

We have constructed a new theranostic system by combining unique aspects of (i) DTPA-Mn(II) complex as a MRI CAs, (ii) BSA as a capturing agent, and (iii) MTX as a chemotherapeutic drug on (iv) RGO-PDA surface as a biocompatible platform, resulted in RGO-PDA-BSA-DTPA-Mn(II)/MTX nanocomposite structure.

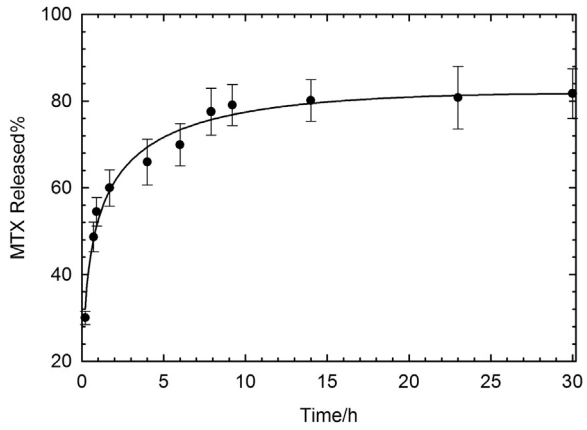

Fig. 5. The MTX release results obtained for RGO-PDA-BSA-DTPA-Mn(II)/MTX system in 0.05 M PBS at pH 7.4 at different time intervals. Error bars are obtained using at least three measurements.

Physicochemical properties of the system, studied by several techniques, supported stability of the immobilized DTPA-Mn(II) complex with an acceptable amount of complexed Mn(II).

The system showed high selectivity for 4T1 cells, originated from both MTX and BSA, neighbored on the RGO-PDA surface in the nanocomposite structure. The immobilized BSA has increased the degree of selectivity of the system for 4T1 cells by a factor of four compared with the system lacking the BSA. This tendency was not hindered by the presence of DTPA-Mn(II) complex contrast agent immobilized on the graphene surface.

Furthermore, the in-vitro release study of MTX showed that about 80% of MTXs have left the system surface during the first 12 h of incubation at pH 7.4.

The non-toxicity of DTPA-Mn(II) system compared with DTPA-Gd (III) based systems, the chemosensitivity of anticancer drug evaluated based on the EIS as a powerful method, besides the multifunctionality and biocompatibility of the system constituents make it a suitable system for theranostic intentions.

Conclusively, the system designed here is general, can provide new and efficient insights to construct and develop different theranostic systems with collection of features for in vivo applications like imaging and chemotherapy. For example, the system can be used for photothermal therapy intention, based on the GO and PDA as photothermal agents, to enhance the sensitivity of chemotherapy and improve therapeutic effects.

Acknowledgment

The authors gratefully acknowledge the University of Isfahan (UI) and Iran National Science Foundation, Vise Presidency for Science and Technology (INSF/VPST), providing grant, and the INSF/VPST Iran High-Tech Laboratory Network (IH-TLN) for supporting the use of high technology facilities and services.

Appendix A. Supporting information

Supplementary data associated with this article can be found in the online version at doi:10.1016/j.bios.2018.07.011.

References

Aravind, A., Jeyamohan, P., Nair, R., Veeranarayanan, S., Nagaoka, Y., Yoshida, Y., Maekawa, T., Sakthi Kumar, D., 2012. Biotechnol. Bioeng. 109, 2920–2931.
Barth, A., 2007. Biochim. Biophys. Acta 1767, 1073–1101.
Bausch, A., Leuenberger, H., 1994. Int. J. Pharm. 101, 63–70.
Burger, K.N.J., Staffhorst, R.W.H.M., de Vijlder, H.C., Velinova, M.J., Bomans, P.H., Frederik, P.M., de Kruijff, B., 2002. Nat. Med. 8, 81–84.
Cheng, C., Nie, S., Li, S., Peng, H., Yang, H., Ma, L., Sun, S., Zhao, C., 2013. J. Mater. Chem. 1, 265–275.
Cheon, Y.A., Bae, J.H., Chung, B.G., 2016. Langmuir 32, 2731–2736.
Ding, G., Jiang, Q., Li, L., Zhang, L., Zhang, Z.G., Ledbetter, K.A., Ewing, J.R., Li, Q., Chopp, M., 2006. Brain Res. 1114, 195–203.
Feng, L.Z., Liu, Z., 2011. Nanomedicine 6, 317–324.
Frei, E., 2011. Diabetol. Metab. Syndr. 3, 1–4.
Gianolio, E., Stefania, R., Di Gregorio, E., Aime, S., 2012. Eur. J. Inorg. Chem. 2012, 1934–1944.
Gu, R., Xu, W.Z., Charpentier, P.A., 2013. J. Polym. Sci. 51, 3941–3949.
Hong, S., Kim, K.Y., Wook, H.J., Park, S.Y., Lee, K.D., Lee, D.Y., Lee, H., 2011. Nanomedicine 6, 793–801.
Hummers, W.S., Offeman, R.E., 1958. J. Am. Chem. Soc. 80 (1339–1339).
Jokerst, J.V., Gambhir, S.S., 2011. Acc. Chem. Res. 44, 1050–1060.
Karimi Shervedani, R., Samiei Foroushani, M., 2014. Bioelectrochemistry 98, 53–63.
Karimi Shervedani, R., Torabi, M., Yaghoobi, F., 2017b. Electrochim. Acta 244, 230–238.
Karimi Shervedani, R., Ansarifar, E., Samiei Foroushani, M., Momenbeak, F., 2017a. Electroanalysis 29, 272–279.
Karimi Shervedani, R., Yaghoobi, F., Torabi, M., Samiei Foroushani, M., 2016. J. Phys. Chem. C 120, 23212–23220.
Ke, H., Wang, J., Dai, Z., Jin, Y., Qu, E., Xing, Z., Guo, C., Yue, X., Liu, J., 2011. Angew. Chem. Int. Ed. 50, 3017–3021.
Kratz, F., 2008. J. Control. Release 132, 171–183.
Kueny-Stotz, M., Garofalo, A., Felder-Flesch, D., 2012. Eur. J. Inorg. Chem. 12, 1987–2005.
Lauffer, R.B., Brady, T.J., 1985. Magn. Reson. Imaging 3, 11–16.
Liu, Y., Ai, K., Lu, L., 2014. Chem. Rev. 114, 5057–5115.
Loving, G.S., Mukherjee, S., Caravan, P., 2013. J. Am. Chem. Soc. 135, 4620–4623.
Lu, Z.R., Ye, F.R., Vaidya, A., 2007. J. Control. Release 122, 269–277.
Mason, S.F., 1955. J. Chem. Phys. 23, 2336–2346.
Ogan, M.D., Schmiedl, U., Moseley, M.E., Grodd, W., Paajanen, H., Brasch, R.C., 1987. Invest. Radiol. 22, 665–671.
Pan, D., Caruthers, S.D., Hu, G., Senpan, A., Scott, M.J., Gaffney, P.J., Wickline, S.A., Lanza, G.M., 2008. J. Am. Chem. Soc. 130, 9186–9187.
Pan, D., Schmieder, A.H., Wickline, S.A., Lanza, G.M., 2011. Tetrahedron 67, 8431–8444.
Peters, T., 1985. Adv. Protein Chem. 37, 161–245.
Pichler, V., Mayr, J., Heffeter, P., Dömötör, O., Enyedy, E.A., Hermann, G., Groza, D., Köllensperger, G., Galanksi, M., Berger, W., Keppler, B.K., Kowol, C.R., 2013. Chem. Commun. 49, 2249–2251.
Schmiedl, U., Ogan, M., Paajanen, H., Marotti, M., Crooks, L.E., Brito, A.C., Brasch, R.C., 1987. Radiology 162, 205–210.
Schwendener, R.A., Wüthrich, R., Duewell, S., Westera, G., von Schulthess, G.K., 1989. Int. J. Pharm. 49, 249–259.
Shen, A.J., Li, D.L., Cai, X.J., Dong, C.Y., Dong, H.Q., Wen, H.Y., Dai, G.H., Wang, P.J., Li, Y.Y., 2012. J. Biomed. Mater. Res. A 100, 2499–2506.
Shilina, Y., Ziv, B., Meir, A., Banerjee, A., Ruthstein, S., Luski, S., Aurbach, D., Halalay, I.C., 2016. Anal. Chem. 88, 4440–4447.
Venkatanarayanan, A., Keyes, T.E., Forster, R.J., 2013. Anal. Chem. 85, 2216–2222.
Wang, D., Gan, N., Zhang, H., Li, T., Qiao, L., Cao, Y., Su, X., Jiang, S., 2015. Biosens. Bioelectron. 65, 78–82.
Xu, L.Q., Yang, W.J., Neoh, K.G., Kang, E.T., Fu, G.D., 2010. Macromolecules 43, 8336–8339.
Yang, K., Feng, L., Liu, Z., 2015. Expert Opin. Drug Deliv. 12, 601–612.
Yang, K., Feng, L., Shi, X., Liu, Z., 2013. Chem. Soc. Rev. 42, 530–547.
Zangmeister, R.A., Morris, T.A., Tarlov, M.J., 2013. Langmuir 29, 8619–8628.
Zhang, M., Cao, Y., Chong, Y., Ma, Y., Zhang, H., Deng, Z., Hu, C., Zhang, Z., 2013. ACS Appl. Mater. Interfaces 5, 13325–13332.